Dalton Transactions

PAPER

Cite this: *Dalton Trans.*, 2017, **46**, 13854

The impact of nitrogen doping and reduced-niobium self-doping on the photocatalytic activity of ultra-thin $Nb_3O_8^-$ nanosheets†

HPSTAR
449-2017

Yannan Zhou,[a,b] Ting Wen,*[a,b] Weiqian Kong,[a,b] Baocheng Yang*[a,b] and Yonggang Wang *[c,d]

Received 14th August 2017,
Accepted 13th September 2017

DOI: 10.1039/c7dt03006a

rsc.li/dalton

Nitrogen doping *via* high-temperature ammonization is a frequently used strategy to extend the light harvesting capacity of wide-bandgap catalysts in the visible region. Under such a reductive atmosphere, the reduction of transition metals is supposed to occur, however, this has not been thoroughly studied yet. Here, by combining chemically-controlled doping and subsequent liquid exfoliation, ultra-thin $[Nb_3O_8]^-$ nanosheets with separate N doping, reduced-Nb doping and N/reduced-Nb codoping were fabricated for comparative studies on the doping effect for photocatalytic hydrogen evolution. Layered KNb_3O_8 was used as the starting material and the above-mentioned three doping conditions were achieved by high-temperature treatment with urea, hydrogen and ammonia, respectively. The morphology, crystal and electronic structures, and the catalytic activity of the products were characterized thoroughly by means of TEM, AFM, XRD, XPS, EPR, absorption spectroscopy and photocatalytic hydrogen evolution. Significantly, the black N/reduced-Nb co-doped monolayer $[Nb_3O_8]^-$ nanosheets exhibit the mostly enhanced photocatalytic hydrogen generation rate, indicating a synergistic doping effect of the multiple chemical-design strategy. The modified electronic structure of $[Nb_3O_8]^-$ nanosheets and the role of exotic dopants in bandgap narrowing are put forward for the rational design of better photocatalysts with reduced-metal self-doping.

Introduction

Light-energy-converting nanomaterials for renewable energy technology, such as water-splitting and decomposition of mostly organic compounds, are currently under intense research.[1–5] Since Fujishima and Honda first reported the hydrogen evolution by photocatalytic water splitting on titanium oxide (TiO_2) electrodes in 1972,[6] abundant materials have been surveyed for this purpose. However, up to now, there are still two challenges in the exploration of practically-usable photocatalytic materials: (1) selective crystal-facet exposure and the creation of a large surface area; (2) efficient light harvesting in the visible region. Various nano-crystallization methods have been developed for the former challenge. While for the latter issue, a frequently adopted strategy is the introduction of exotic excitation states, *i.e.* either elemental doping or construction of hetero-structures. The doping method includes single-elemental doping,[7–9] codoping with two or more foreign elements[10] and reduced metal self-doping (such as the defective TiO_2 [11,12]). Besides the narrowing of the bandgap, these efforts can also increase the lifetime of photo-generated electron–hole pairs.

In recent decades, Ti/Nb/Ta based layered perovskites with a wide variety of structural and electronic properties have been attracting considerable attention as photocatalytic materials, such as $La_2Ti_2O_7$,[13] $KNbO_3$,[14] KNb_3O_8,[15–17] $KTiNbO_5$,[7,18–21] and $CsCa_2Ta_3O_{10}$.[22] Liquid exfoliation of these layered perovskites can yield ultrathin two-dimensional nanosheets, which are regarded as a new type of nanoscale materials with peculiar features of both molecular thickness and extremely high 2D anisotropy.[23–25] For example, HNb_3O_8 nanosheets have been reported to have enhanced activity in the photo-

---

[a] *Institute of Nanostructured Functional Materials, Huanghe Science and Technology College, Zhengzhou, Henan 450006, China. E-mail: tingwen@infm.hhstu.edu.cn, baochengyang@hhstu.infmm.cn*

[b] *Henan Provincial Key Laboratory of Nano-composite and Applications, Zhengzhou 450006, Henan Province, China*

[c] *Center for High Pressure Science and Technology Advanced Research (HPSTAR), Beijing 100094, China. E-mail: yonggang.wang@hpstar.ac.cn*

[d] *HPSynC, Geophysical Laboratory, Carnegie Institution of Washington, Argonne, IL 60439, USA*

† Electronic supplementary information (ESI) available: XRD patterns for acid-exchanged phases and SEM images of KNO, KNO-**1**, KNO-**2**, and KNO-**3**; XRD, UV adsorption, EDS, HRTEM and SAED of nanosheet colloidal suspension images; hydrogen evolution by photocatalytic water splitting of KNO-**3** with light irradiation at 405 nm. See DOI: 10.1039/c7dt03006a

catalytic field.[26–30] $[Nb_3O_8]^-$ nanosheets were fabricated *via* chemical exfoliation of KNb_3O_8 and the obtained nanosheet films possess enhanced photocatalytic oxidation activity which was evaluated using methylene blue.[31] Wu *et al.* reported the dramatically-enhanced photocatalytic hydrogen evolution performance in ultra-thin HNb_3O_8 nanosheets benefiting from their unique surface-structure features.[17] If one can combine the liquid exfoliation of layered perovskites with the above-mentioned doping strategies, a large surface area together with effective utilization of visible light may be achieved in a given layered perovskite catalyst at the same time. One pioneering study is the fabrication of Rh-doped calcium niobate nanosheets with high photocatalytic activity for H_2 production from a water/methanol system without any cocatalyst loading.[32] However, such joint attempts have been rarely reported until now.

Nitrogen doping *via* high-temperature ammonization is a frequently used strategy to extend the light harvesting capacity of wide-bandgap catalysts into the visible region. Under such a reducing atmosphere, the reduction of transition metals is supposed to occur, however, this has not been thoroughly studied yet. In this work, we present the structure and electronic analysis of ultra-thin $[Nb_3O_8]^-$ nanosheets with three different doping situations, that is, nitrogen doping, reduced-Nb (*r*Nb) self-doping and nitrogen/*r*Nb codoping. These photocatalysts were fabricated *via* different treatment routes adopting urea as the N source, or under H_2 or ammonium atmospheres, respectively. The products enable a comparative study on the effect of elemental doping on the bandgap narrowing and photocatalytic performance of ultra-thin $[Nb_3O_8]^-$ nanosheets. Experimental evidence showed a synergistic effect of N-doping and low-valence-Nb self-doping in black N/*r*Nb-$[Nb_3O_8]^-$ nanosheets. These results are suggestive of the rational design of better reduced-metal self-doped photocatalysts.

Experimental

Materials

The starting materials are potassium carbonate (K_2CO_3, 99.9%), niobium oxide (Nb_2O_5, 99.99%), hydrochloric acid (HCl, 36.5%), 40% tetrabutyl ammonium hydroxide (TBAOH) and $H_2PtCl_6·6H_2O$ (99.9%, Aldrich).

Synthesis of KNb_3O_8 precursors

K_2CO_3 and Nb_2O_5 were mixed in a molar ratio of 1.05 : 3, and heated at 600 °C for 2 h and then at 900 °C for 3 h. An excess of alkali metal carbonate was added to compensate for the loss due to volatilization of the alkali component.

Selective elemental doping

1 g of KNb_3O_8 was finely milled with 2 g of urea (mass ratio = 1 : 2) and then the resulting mechanical mixture was heated in air at 400 °C for 5 h. This N-doped KNb_3O_8 is denoted as KNO-**1**. Comparatively, *r*Nb-doped KNb_3O_8 was calcined at 800 °C under a H_2/N_2 (H_2: 5 vol%) flow (denoted as KNO-**2**) and N/*r*Nb-codoped KNb_3O_8 was calcined at 800 °C under NH_3 (60 mL min^{-1}) for 5 h (denoted as KNO-**3**).

Liquid exfoliation of the $[Nb_3O_8]^-$ nanosheets

The as-prepared specimens were converted to the protonated forms by acid exchange with 2 M HCl for a week. After the proton exchange, the powder was washed three times and then centrifuged. The protonated form of samples (1.0 g) was treated with TBAOH aqueous solution. The concentration of TBAOH was adjusted to set a molar ratio of TBA^+/H^+ at 1 where H^+ denotes exchangeable protons in the solid. This mixture was stirred at room temperature for two weeks. The colloidal suspensions thus obtained were centrifuged at 1500 rpm for 5 min to separate a small amount of unexfoliated residue. The nanosheets were restacked into lamellar flocculates by adding their colloidal suspensions to 2 M HCl solution at a speed of 1 cm^3 min^{-1}.

Characterization

The powder X-ray diffraction (PXRD) patterns of all the samples were collected at room temperature on a Bruker D8 Advance diffractometer using a germanium monochromator (Cu-Kα radiation, 40 kV and 40 mA). The data for phase identification were obtained in the 2 theta range between 5° and 70° and with the remaining time of 0.1 s per step. Scanning electron microscopy (SEM) images were recorded using a Quanta 250 FEG FEI at 30 kV in gentle-beam mode without any metal coating. Energy dispersive spectroscopy (EDS) and elemental mapping were recorded on the same SEM equipment. Transmission electron microscopy (TEM) images and high-resolution transmission electron microscopy (HRTEM) images were recorded on a Tecnai G2 20 TEM with an accelerating voltage of 200 kV using a carbon-coated copper grid to obtain detailed insight into the microsphere morphology. UV-vis diffuse reflectance spectra were recorded by using a U-4100 UV-Vis-NIR spectrometer (Hitachi). The platinum content of the photocatalysts was determined by ICP-OES (Optima2000DV, USA). X-ray photoelectron spectroscopy (XPS) data were obtained by using a photoelectron spectrometer using an Al Kα X-ray source (Axis Ultra DLD, Kratos). The electron paramagnetic resonance (EPR) spectra were collected using a Bruker ER200-SRC spectrometer at 77 K. The room temperature X-ray Absorption Spectra (XAS) on the Nb K-edge (18.986 keV) of all the samples were collected at 16BM-D, Advanced Phonon Source, Argonne National Laboratory. The data were processed and fitted with the program Athena.[33]

Photocatalytic activity tests

In order to clarify the photocatalytic properties of the nanosheets, photocatalytic hydrogen evolution was performed on their lamellar flocculates. The photocatalytic reactions were carried out under both full arc and visible light irradiation (420 nm cut-off filter) in a closed photo-reactor using a 300 W Xe lamp. The rate of H_2 production was measured in an aqueous solution (100 mL) containing 50–100 mg of catalyst and 20 vol% methanol. H_2 gas was analyzed by gas chromatography (TCD, nitrogen as a carrier gas and a 5 Å molecular sieve column). Co-catalysts were photodeposited on nanosheets with 20 vol% methanol aqueous solution (100 mL of nanosheet suspension, 40 mL of methanol, 30 mL of water) containing $H_2PtCl_6 \cdot 6H_2O$ by irradiation with the 300 W Xe lamp for 3 h. To investigate the stability of the catalysts, the specimen after one trial was washed and dried for the subsequent recycling test. The apparent quantum efficiency (QE) was measured under the same photocatalytic reaction conditions with light irradiation at 405 nm by using combined band-pass and cut-off filters (QD405) and 300 W Xe lamps. The AQE was calculated using the following equation:

$$\mathrm{AQE} = (N(\mathrm{H_2}) \times 2)/N(\mathrm{photons}) \times 100\%$$

Electrochemical measurements

Photocurrent and EIS impedance measurements were performed on an electrochemical workstation (Shanghai). The samples were coated on FTO glasses and immersed in 1 M KOH aqueous solution for measurements.

Results and discussion

Characterization of KNO-1, KNO-2 and KNO-3

There are four samples in this study: undoped KNb_3O_8 (KNO), N-doped KNb_3O_8 (KNO-**1**), *r*Nb-doped KNb_3O_8 (KNO-**2**) and N/*r*Nb-codoped KNb_3O_8 (KNO-**3**). They are obtained by a direct solid state reaction, treatment of the pristine KNO with urea, and annealing under an H_2 and NH_3 atmosphere, respectively. The phase purity of all the products was confirmed by the successful indexing of the PXRD patterns (Fig. 1), which are in good agreement with the previous studies.[28,34] The pristine KNb_3O_8 crystallizes in a layered perovskite-type structure with the orthorhombic space group *Amam*, and the three subsequent doping processes do not affect the crystal structure much as visually evidenced from the PXRD patterns. The unit cell parameters were obtained through LeBail fitting of the PXRD data. Compared to KNO, KNO-**1** and KNO-**2**, KNO-**3** shows only a slight shrinkage in the *ab* plane (Fig. 1b), which implies that: (a) nitrogen partially substituted oxygen in the layered niobates without altering the crystal phase; (b) the N-doping in the perovskite layer may be different in the two samples KNO-**1** and KNO-**3**, and this will be discussed later in association with the XPS analyses. The H^+-exchanged samples show sharper (0*k*0) diffractions compared with their precursors (Fig. S1†), reflecting the more obvious preferred orientation for the products. The interlayer space (d_{020}) of KNO, KNO-**2** and KNO-**3** expanded from 10.60 Å to 11.27 Å approximately except for that of KNO-**1** (12.37 Å), which may be attributed to the intercalation of water molecules into the interlayer space. The restacked nanosheets exhibited weaker and broader in-plane diffraction peaks due to the turbostratic disorder restacking and the loss of periodicity in the *b* axis (Fig. S2†). The EDS and elemental mapping measurement results before and after the exfoliation–restacking process further confirm the components of the $[Nb_3O_8]^-$ nanosheets (Fig. S3†).

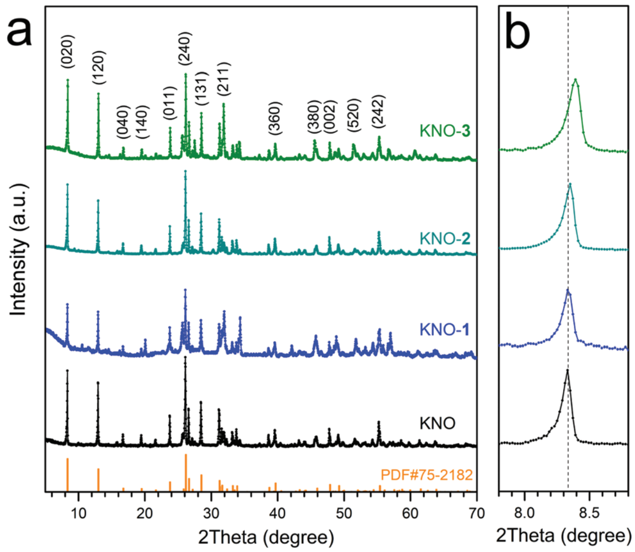

Fig. 1 (a) XRD patterns of KNO, KNO-**1**, KNO-**2**, and KNO-**3** samples. (b) Detailed XRD pattern in a low angle range showing the (020) peak shift.

Elemental doping is proven to be an efficient way to change the bandgap of semiconductors. In contrast to the white KNO precursor, the doped products KNO-**1**, KNO-**2** and KNO-**3** exhibit yellow, gray and black colours, respectively. The light harvesting capacities of KNO and the three doped samples were studied by UV-vis DRS measurements (as shown in Fig. 2). A sharp absorption edge around 300 nm is observed for KNO corresponding to the Nb–O charge transfer transition. Both N doping and *r*Nb self-doping can shift the bandgap position of KNO to a longer wavelength. Specifically, the *r*Nb self-doped KNO-**2** and KNO-**3** samples exhibit high absorption backgrounds in the whole visible range compared with those of KNO and KNO-**1**, which can be attributed to the intermediate energy levels introduced by the oxygen vacancies.[35–37] The oxygen vacancies (or in other words, *r*Nb) can be formed due to the reduction of Nb^{5+} under reducing H_2 or NH_3 atmospheres.[38–40] As for the NH_3-treated black KNO-**3** sample, an obviously red-shifted bandgap together with a broad absorption over the entire UV-visible range is highly expected to favour the photocatalytic performance under visible light irridiation.[17,35,36] Fig. 2b presents the plot for the square of absorption efficiency (α) multiplied by the photoenergy $(\alpha h\nu)^2$ *versus* the photoenergy (E). KNO is reported as a direct bandgap semiconductor. The bandgaps for KNO, KNO-**1**, KNO-**2** and KNO-**3** are estimated to be 3.24, 2.93, 3.16 and 2.72 eV, respectively. In addition, no obvious change in the shape and size of the samples was detected as evidenced by the SEM images (Fig. S4†), indicating that the layered perovskite structure was sustained during the doping processes. The UV-visible absorption spectra of the restacked $[Nb_3O_8]^-$ nanosheets differ a lot from those of the parent layered solids (Fig. S5†). The blue-shifts compared to those of the parent materials are due to a quantum-confinement effect.

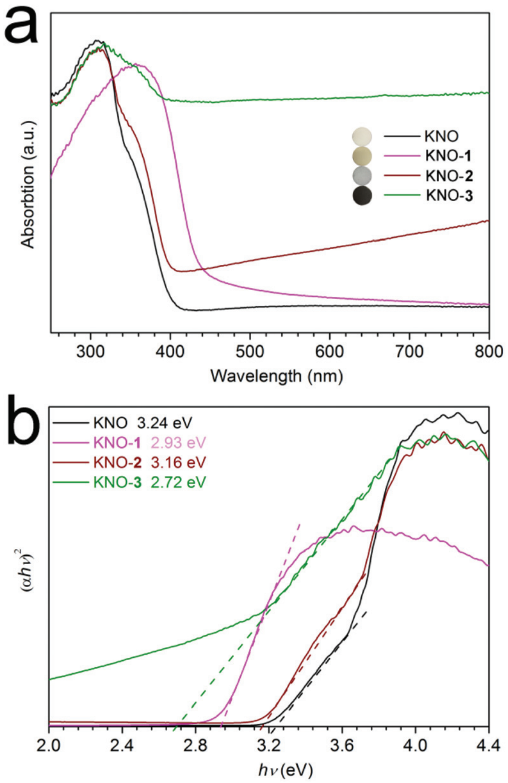

Fig. 2 (a) UV-vis absorption spectra and (b) the derived bandgap based on the Kubelka–Munk function of KNO, KNO-**1**, KNO-**2**, and KNO-**3** samples. The insets of (a) show the photographs of the samples.

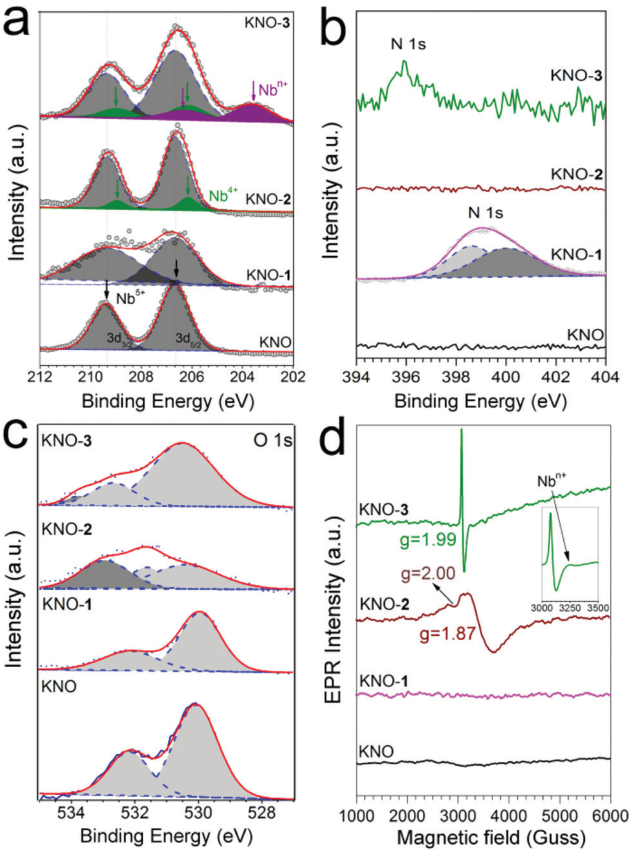

Fig. 3 (a) Nb 3d, (b) N 1s, and (c) O 1s XPS spectra for KNO, KNO-**1**, KNO-**2** and KNO-**3** samples. (d) 77 K EPR spectra for KNO, KNO-**1**, KNO-**2** and KNO-**3** samples.

To investigate the chemical states of niobium and nitrogen, high resolution XPS measurements on the Nb 3d and N 1s edges were conducted (as shown in Fig. 3). Both KNO and KNO-**1** show two peaks centred at 209.38 and 206.68 eV, corresponding typically to the Nb $3d_{3/2}$ and $3d_{5/2}$ peaks for Nb^{5+} surrounded by six oxygen atoms. While for KNO-**2** and KNO-**3**, these peaks shift to lower binding energies visually. The two emerging XPS bands located at around 208.98 and 206.18 eV for KNO-**2** and KNO-**3** could be assigned to the Nb^{4+} species.[41–43] In addition to the Nb^{4+} XPS peaks, other two low-energy peaks around 206.38 and 203.68 eV observed for KNO-**3** indicate the formation of *r*Nb ions with chemical valence even lower than +4.[44–46] Fig. 3b presents the N 1s peaks of the samples, in which KNO-**3** shows obvious N 1s peaks at 396.08 eV, whereas the N 1s peaks of KNO-**1** could be decomposed to two component peaks centered at approximately 398.68 eV and 399.98 eV. The slightly different XPS positions may be attributed to the distinct chemical coordination environments of N in KNO-**1** and KNO-**3** considering their different preparation methods. Similar differences for the N XPS peaks were observed in the previous N-doped photocatalysts,[7,47,48] where the low-energy N peaks were assigned to the covalently-bonded metal-N within the host lattice and the higher-energy peaks around 399.98 eV were assumed to arise partially from absorbed N_2 (γ-N_2). However, in the cases of KNO-**1** and KNO-**3**, the difference of the N XPS positions may also arise from the different oxidation states of Nb in the two samples.[49] The O 1s peaks of KNO and KNO-**1** are fitted by two peaks at 530.8 and 532.18 eV (Fig. 3c), and are related to the lattice oxygen and other components such as O_2 and H_2O adsorbed on the surface of catalysts, respectively. A high-BE peak at 532.88 eV corresponding to O in oxygen-deficient regions can be observed for KNO-**2** and KNO-**3** due to the reduced atmosphere.

To clarify the formation of low-valence *r*Nb, low-temperature EPR measurements for all the samples were conducted at 77 K (as shown in Fig. 3d). No peak was observed in the 1000–7000 Gauss region for KNO and KNO-**1**, indicating the absence of low-valence Nb ions. KNO-**2** shows EPR signals at g = 1.87 and 2.00, which can be attributed to the presence of Nb^{4+} and the oxygen vacancy, respectively.[37,41–43] An additional weak broad signal from g = 1.86 appears in the black KNO-**3**, which can be assigned to the Nb^{n+} (n < 4) species in the surface layer. Another difference between KNO-**2** and KNO-**3** is the enhanced sharpness and the larger g value (1.99) of Nb^{4+} peaks in KNO-**3**. These EPR results further confirm that the thermal treatment of KNO under a reductive NH_3 atmosphere is not only an efficient method for nitrogen doping, but also favours the self-doping of low-valence Nb.

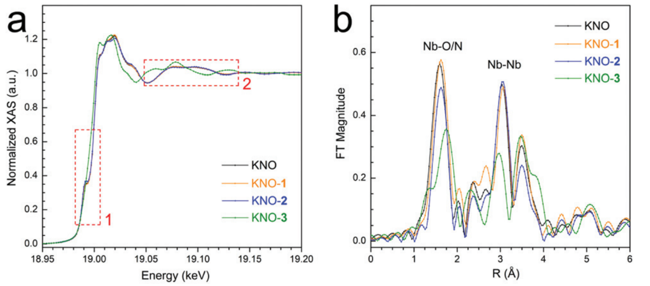

Fig. 4 (a) Normalized Nb K-edge XAS data for KNO, KNO-**1**, KNO-**2** and KNO-**3**. (b) Fourier transformed profiles showing the vibration of Nb–O/N and Nb–Nb bond lengths.

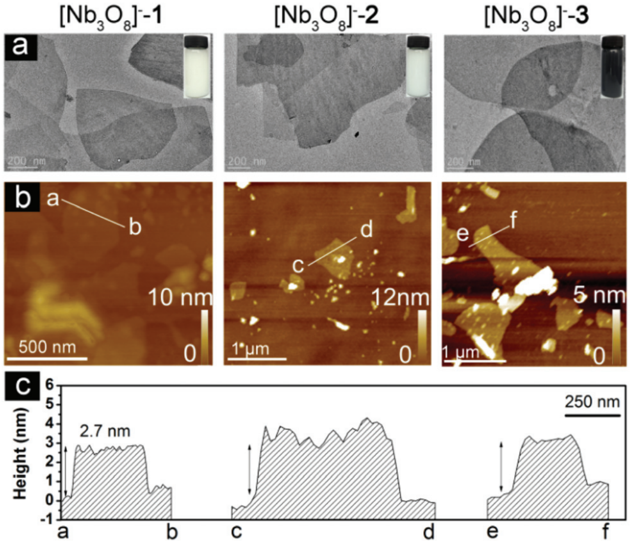

Fig. 5 (a) TEM, (b) AFM images, and (c) cross-sectional profile of $[Nb_3O_8]^-$-**1**, $[Nb_3O_8]^-$-**2**, and $[Nb_3O_8]^-$-**3**. The insets of (a) present the photographs of their suspensions in aqueous solution.

XAS measurements on the Nb K-edge (18.986 keV) of all the samples were conducted to probe the local structure evolution of KNO during the various doping processes (as shown in Fig. 4). There are two obvious changes in the XAS spectra for KNO, KNO-**1**, KNO-**2** and the NH_3-treated KNO-**3**. Firstly, an obvious increase of the pre-edge peak is observed for KNO-**3**, compared with only a slight increase of KNO-**2** corresponding to those of KNO and KNO-**1**. The increase of the pre-edge (or edge position shift) can be attributed to the partial reduction of Nb^{5+} to Nb^{4+} for KNO-**2** and Nb^{n+} ($n \leq 4$) for KNO-**3**, respectively.[50,51] Secondly, the distinct features in the near- and extended- edge region indicate a noticeable local structure change surrounding the Nb centers in NH_3-treated KNO-**3**. Fig. 4b presents the FT magnitudes *versus* atomic distances derived from the extended-edge XAS data, which can reflect the typical Nb–O/N and Nb–Nb distances. Compared with that of the pristine KNO and KNO-**1**, KNO-**2** shows a slight decrease of the nearest Nb–O/N surrounding, which indicates the formation of oxygen vacancies during the H_2-reduction process.[52] Comparatively, KNO-**3** shows obvious decreases of both Nb–O/N and Nb–Nb bond lengths, which not only indicates the formation of more oxygen defects but also shrinkage of the perovskite layer. This XAS evidence is also consistent with the XPS and EPR analyses.

Fig. 5 represents the TEM and AFM images of the exfoliated $[Nb_3O_8]^-$ nanosheets from the corresponding bulky precursors. The nanosheets show a clear unilamellar feature due to their layered perovskite structures. Liquid exfoliation does not affect the optical absorption behaviours of the four samples since the suspensions of their nanosheets still exhibit yellow, grey and black for $[Nb_3O_8]^-$-**1**, $[Nb_3O_8]^-$-**2** and $[Nb_3O_8]^-$-**3**, respectively (as shown in the inset of Fig. 5). The cross-sectional profiles of the AFM images prove their thickness to be about 2.7 nm, which is close to the single-molecular thickness of the $[Nb_3O_8]^-$ layer plus TBA^+ ions on the surface. In the HRTEM images (Fig. S6†), typical lattice fringes with spacing values of 0.41 nm are observed for the three thermal-treated samples, which match well with the (220) plane of orthorhombic KNO. SAED patterns also reveal the single crystal nature of the nanosheets. The diffraction spots with *d* values of 0.530, 0.205 and 0.223 nm are observed, all of which can be well indexed into the (040), (440) and (400) planes of orthorhombic KNO.

Photocatalytic activity and stability

The photocatalytic H_2 production activities of the as-prepared samples were evaluated under full arc irradiation in the presence of CH_3OH (as shown in Fig. 6). Compared with the individually N or *r*Nb doped $[Nb_3O_8]^-$ products, N/*r*Nb codoped $[Nb_3O_8]^-$-**3** nanosheets show a higher H_2 evolution rate of 449.9 µmol h^{-1}. Nevertheless, the H_2 evolution under visible irradiation was almost negligible, in good agreement with the previous report.[22,52] After Pt loading, the hydrogen evolution rate can be further improved to 589.2 µmol h^{-1}. The actual loading of Pt was determined to be 0.45–0.47 wt% (0.5 wt% nominal loading) by ICP-OES. After reaction, Pt nanoparticles on the $[Nb_3O_8]^-$ nanosheets show good stability as confirmed by the ICP-OES results (Table S1†). These results not only

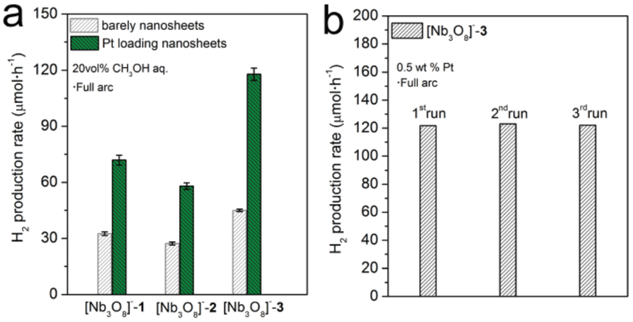

Fig. 6 (a) Comparison of the hydrogen evolution rate of barely (100 mg) or Pt loading (50 mg) nanosheets under full arc irradiation. (b) Cycling performance of $[Nb_3O_8]^-$-**3** nanosheets (0.5 wt% Pt) for H_2 evolution at regular intervals (4 h). The amount of catalyst: 50 mg.

reveal the separate impacts of N doping, *r*Nb self-doping and N/*r*Nb codoping on the photocatalytic performance of such perovskite nanosheets, but also demonstrate the superiority of ammoniation of Nb-based semiconductors that can introduce N and *r*Nb doping at the same time. Fig. 6b presents the cycling performance of the optimized $[Nb_3O_8]^-$-**3** nanosheets on photocatalytic H_2 production. After three cycles, no noticeable decrease of the H_2 production rate was observed for the $[Nb_3O_8]^-$-**3** nanosheets, proving the high stability of the dually-doped $[Nb_3O_8]^-$ nanosheets. Fig. S7† shows the time courses of H_2 evolution from aqueous 20 vol% methanol solutions in the presence of 25 mg of $[Nb_3O_8]^-$-**3** nanosheets with light irradiation at 405 nm by using combined band-pass and cut-off filters (QD405) and 300 W Xe lamps. The QE of the optimized $[Nb_3O_8]^-$-**3** nanosheets is found to be 1.69% at 405 nm.

Electrochemical measurements

For further investigation, the electrical properties and the charge transfer process of KNO nanosheets with different doping routes, the photocurrent responses and EIS spectra were determined at open circuit potential under a solar light simulating source (Xe lamp, AM 1.5G, 100 mW cm^{-2}). Fig. 7a shows a sequence of $[Nb_3O_8]^-$-**3** > $[Nb_3O_8]^-$-**1** > $[Nb_3O_8]^-$-**2** for the samples, which is consistent with the hydrogen production results. As to the EIS spectra (Fig. 7b), a decrease of the charge transfer resistance indicates a fast interfacial charge transfer process. The $[Nb_3O_8]^-$-**3** photoanode indicates a smaller charge transfer resistance, which demonstrates that the separation efficiency of $[Nb_3O_8]^-$-**3** can be effectively improved by N/*r*Nb codoping.

Impact of N/*r*Nb codoping on the band gap tuning

The positions of the conduction band minimum (CBM) and the valence band maximum (VBM) were estimated following the calculation method developed by Xu *et al.*[53] (as shown in Fig. 8; for details, see the ESI†). Furthermore, based on the results of our experiments, the impacts of N doping, *r*Nb self-doping and N/*r*Nb codoping on the electronic structure of KNO are presented in Fig. 8. Nitrogen doping can undoubtedly introduce an impurity energy level just above the valence band (VB) of the KNO perovskite (the case of KNO-**1**).[54] The measured bandgap is 2.93 eV compared with that of 3.24 eV for the bare KNO. While for KNO-**2**, the reduced Nb^{4+} introduces an intermediate energy level just below the conducting band of the KNO perovskite, and the band gap value is 3.16 eV. Simultaneous N/*r*Nb codoping in KNO-**3** introduces not only both N^{3-} and Nb^{4+} intermediate energy levels, but also an exotic Nb^{n+} ($n < 4$) level that can further narrow the bandgap of the material. These results favour the enhancement of photo-absorption of $[Nb_3O_8]^-$ nanosheets in the whole UV-visible region as well as the charge separation during the photocatalytic process.[11,55,56] Thus the high-temperature ammoniation of Nb-based semiconductors is demonstrated as an efficient strategy to improve the photocatalytic performance of layered perovskite materials.

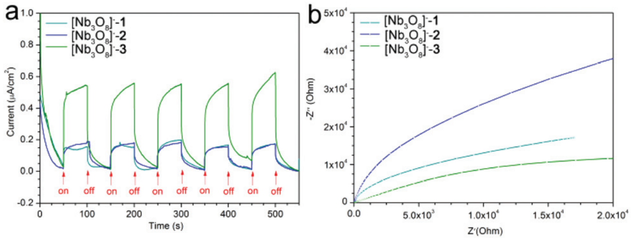

Fig. 7 (a) Photocurrent of $[Nb_3O_8]^-$-**1**, $[Nb_3O_8]^-$-**2**, and $[Nb_3O_8]^-$-**3** nanosheets *versus* time at a bias of 0.6 V under simulated sunlight irradiation (AM 1.5). (b) EIS Nyquist plots of $[Nb_3O_8]^-$-**1**, $[Nb_3O_8]^-$-**2**, and $[Nb_3O_8]^-$-**3** nanosheets at a bias of 0.2 V without irradiation.

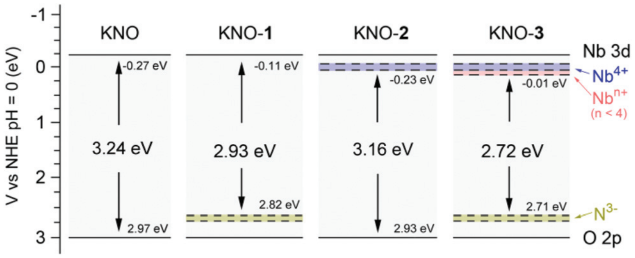

Fig. 8 Assumed band structures of KNO, KNO-**1**, KNO-**2**, and KNO-**3**.

Conclusions

In summary, ultra-thin $[Nb_3O_8]^-$ nanosheets with separate N, *r*Nb self-doping and N/*r*Nb codoping were fabricated under controllable atmospheres followed by subsequent liquid exfoliation. A comparative analysis was performed on the effect of element doping on the bandgap narrowing and the photocatalytic activity of $[Nb_3O_8]^-$ nanosheets. Compared with N doping and *r*Nb self-doping, a synergistic effect was observed in the N/*r*Nb codoped $[Nb_3O_8]^-$ nanosheets, which could be attributed to the dually-inserted energy levels of N^{3-} and *r*Nb ions. The optimized black N/*r*Nb codoped $[Nb_3O_8]^-$ nanosheets exhibit the highest H_2 production rate of 449.9 μmol h^{-1} without any cocatalyst. On the basis of these results, we are confident to conclude that the high temperature ammoniation of Nb-based semiconductors is an efficient route to reduced-metal self-doped photocatalysts.

Conflicts of interest

There are no conflicts to declare.

Acknowledgements

This work is supported by the National Natural Science Foundation of China (21301063, 51472102) and the Natural Science Foundation of Education Department of Henan

Province (12B150015). HPCAT operations are supported by DOE-NNSA under Award No. DE-NA0001974 and DOE-BES under Award No. DE-FG02-99ER45775, with partial instrumentation funding by NSF. APS is supported by DOE-BES, under Contract No. DE-AC02-06CH11357.

Notes and references

1 X. Chen, S. Shen, L. J. Guo and S. S. Mao, *Chem. Rev.*, 2010, **110**, 6503–6570.
2 K. Maeda, *J. Photochem. Photobiol., C*, 2011, **12**, 237–268.
3 X. Chen, C. Li, M. Grätzel, R. Kostecki and S. S. Mao, *Chem. Soc. Rev.*, 2012, **41**, 7909–7937.
4 T. Hisatomi, J. Kubota and K. Domen, *Chem. Soc. Rev.*, 2014, **43**, 7520–7535.
5 X. Li, J. Yu and M. Jaroniec, *Chem. Soc. Rev.*, 2016, **45**, 2603–2636.
6 K. Fujishima and A. Honda, *Nature*, 1972, **238**, 37–38.
7 Z. Zhai, C. Hu, X. Yang, L. Zhang, C. Liu, Y. Fan and W. Hou, *J. Mater. Chem.*, 2012, **22**, 19122–19131.
8 Y. Matsumoto, M. Koinuma, Y. Iwanaga, T. Sato and S. Ida, *J. Am. Chem. Soc.*, 2009, **131**, 6644–6645.
9 X. Zong, C. Sun, Z. Chen, A. Mukherji, H. Wu, J. Zou, S. C. Smith, G. Q. Lu and L. Wang, *Chem. Commun.*, 2011, **47**, 6293–6295.
10 H. Pan, Y. Zhang, V. B. Shenoy and H. Gao, *J. Phys. Chem. C*, 2011, **115**, 12224–12231.
11 G. Wang, H. Wang, Y. Ling, Y. Tang, X. Yang, R. C. Fitzmorris, C. Wang, J. Z. Zhang and Y. Li, *Nano Lett.*, 2011, **11**, 3026–3033.
12 Y. H. Hu, *Angew. Chem., Int. Ed.*, 2012, **51**, 12410–12412.
13 F. Meng, S. K. Cushing, J. Li, S. Hao and N. Wu, *ACS Catal.*, 2015, **5**, 1949–1955.
14 A. Dias, S. Lima, D. Carriazo, V. Rives, M. Pillinger and A. Valente, *J. Catal.*, 2006, **244**, 230–237.
15 S. Liang, L. Wen, S. Lin, J. Bi, P. Feng, X. Fu and L. Wu, *Angew. Chem., Int. Ed.*, 2014, **53**, 2951–2955.
16 J. Xiong, Y. Liu, S. Liang, S. Zhang, Y. Li and L. Wu, *J. Catal.*, 2016, **342**, 98–104.
17 J. Xiong, L. Wen, F. Jiang, Y. Liu, S. Liang and L. Wu, *J. Mater. Chem. A*, 2015, **3**, 20627–20632.
18 C. Liu, R. Han, H. Ji, T. Sun, J. Zhao, N. Chen, J. Chen, X. Guo, W. Hou and W. Ding, *Phys. Chem. Chem. Phys.*, 2016, **18**, 801–810.
19 C. Liu, L. Wu, J. Chen, J. Liang, C. Li, H. Ji and W. Hou, *Phys. Chem. Chem. Phys.*, 2014, **16**, 13409–13417.
20 Z. Zhai, X. Yang, L. Xu, C. Hu, L. Zhang, W. Hou and Y. Fan, *Nanoscale*, 2012, **4**, 547–556.
21 Z. Zhai, Y. Huang, L. Xu, X. Yang, C. Hu, L. Zhang, Y. Fan and W. Hou, *Nano Res.*, 2011, **4**, 635–647.
22 S. Ida, Y. Okamoto, M. Matsuka, H. Hagiwara and T. Ishihara, *J. Am. Chem. Soc.*, 2012, **134**, 15773–15782.
23 Y. Liu, J. Xiong, S. Luo, R. Liang, N. Qin, S. Liang and L. Wu, *Chem. Commun.*, 2015, **51**, 15125–15128.
24 Y. Liu, J. Xiong, Y. Yang, S. Luo, S. Zhang, Y. Li, S. Liang and L. Wu, *Appl. Catal., B*, 2017, **203**, 798–806.
25 S. Zhu, S. Liang, J. Bi, M. Liu, L. Zhou, L. Wu and X. Wang, *Green Chem.*, 2016, **18**, 1355–1363.
26 X. Liu, W. Que and L. B. Kong, *J. Alloys Compd.*, 2015, **627**, 117–122.
27 K. Akatsuka, G. Takanashi, Y. Ebina, N. Sakai, M. Haga and T. Sasaki, *J. Phys. Chem. Solids*, 2008, **69**, 1288–1291.
28 S. Suzuki, K. Teshima, A. Yamaguchi, K. Yubuta, T. Shishido and S. Oishi, *CrystEngComm*, 2012, **14**, 987–992.
29 T. Shibata, G. Takanashi, T. Nakamura, K. Fukuda, Y. Ebina and T. Sasaki, *Energy Environ. Sci.*, 2011, **4**, 535–542.
30 G. Yin, M. Nishikawa, Y. Nosaka, N. Srinivasan, D. Atarashi and E. Sakai, *ACS Nano*, 2015, **9**, 2111–2119.
31 A. Kudo and T. Sakata, *Chem. Lett.*, 1994, **23**, 2179–2182.
32 Y. Okamoto, S. Ida, J. Hyodo, H. Hagiwara and T. Ishihara, *J. Am. Chem. Soc.*, 2011, **133**, 18034–18037.
33 B. Ravel and M. Newville, *J. Synchrotron Radiat.*, 2005, **12**, 537–541.
34 M. A. Bizeto, A. L. Shiguihara and V. R. L. Constantino, *J. Mater. Chem.*, 2009, **19**, 2512–2525.
35 X. Li, N. Kikugawa and J. Ye, *Adv. Mater. Res.*, 2008, **20**, 3816–3819.
36 X. Li, N. Kikugawa and J. Ye, *Chem. – Eur. J.*, 2009, **15**, 3538–3545.
37 G. Li, J. Li, G. Li and G. Jiang, *J. Mater. Chem. A*, 2015, **3**, 22073–22080.
38 M. Miyauchi, M. Takashio and H. Tobimatsu, *Langumir*, 2004, **20**, 232–236.
39 B. Siritanaratkul, K. Maeda, T. Hisatomi and K. Domen, *ChemSusChem*, 2011, **4**, 74–78.
40 Y. Zhou, Y. Wang, T. Wen, B. Chang, Y. Guo, Z. Lin and B. Yang, *J. Colloid Interface Sci.*, 2016, **461**, 185–194.
41 C. Zhou, Y. Zhao, L. Shang, Y. Cao, L. Z. Wu, C. H. Tung and T. Zhang, *Chem. Commun.*, 2014, **50**, 9554–9556.
42 J. Wang, X. Wang, Z. Cui, B. Liu and M. Cao, *Phys. Chem. Chem. Phys.*, 2015, **17**, 14185–14192.
43 B. J. C. Gillot, J. P. Michenaud and M. Maglione, *Solid State Commun.*, 1992, **84**, 1033–1038.
44 X. Pan, M. Yang, X. Fu, N. Zhang and Y. Xu, *Nanoscale*, 2013, **5**, 3601–3614.
45 X. Liu, S. Sadaf, M. Son, J. Shin, J. Park, J. Lee, S. Park and H. Hwang, *Nanotechnology*, 2011, **22**, 475702.
46 X. Jia, L. Kang, X. Liu, Z. Wang, B. Jin, S. Mi, J. Chen, W. Xu and P. Wu, *IEEE Trans. Appl. Supercond.*, 2013, **23**, 2300704.
47 R. Asahi, T. Morikawa, T. Ohwaki, K. Aoki and Y. Taga, *Science*, 2001, **293**, 269–271.
48 J. Fang, F. Wang, K. Qian, H. Bao, Z. Jiang and W. Huang, *J. Phys. Chem. C*, 2008, **112**, 18150–18156.
49 S. Hoang, S. P. Berglund, N. T. Hahn, A. J. Bard and C. B. Mullins, *J. Am. Chem. Soc.*, 2012, **134**, 3659–3662.
50 M. Nakayama, K. Imaki, W. Ra, H. Ikuta, Y. Uchimoto and M. Wakihara, *Chem. Mater.*, 2003, **15**, 1728–1733.

51 R. Kodama, Y. Terada, I. Nakai, S. Komaba and N. Kumagai, *J. Electrochem. Soc.*, 2006, **153**, A583–A588.
52 Y. Zhou, T. Wen, Y. Guo, B. Yang and Y. Wang, *RSC Adv.*, 2016, **6**, 64930–64936.
53 Y. Xu and M. A. A. Schoonen, *Am. Mineral.*, 2000, **85**, 543–556.
54 T. Takata and K. Domen, *J. Phys. Chem. C*, 2009, **113**, 19386–19388.
55 L. Jing, B. Xin, F. Yuan, L. Xue, B. Wang and H. Fu, *J. Phys. Chem. B*, 2006, **110**, 17860–17865.
56 J. Wang, P. Liu, X. Fu, Z. Li, W. Han and X. Wang, *Langmuir*, 2009, **25**, 1218–1223.